applied sciences

MDPI

*Article*

# Two-Phase Non-Newtonian Pulsatile Blood Flow Simulations in a Rigid and Flexible Patient-Specific Left Coronary Artery (LCA) Exhibiting Multi-Stenosis

**Abdulgaphur Athani [1], Nik Nazri Nik Ghazali [1,*], Irfan Anjum Badruddin [2,*], Abdullah Y. Usmani [3], Sarfaraz Kamangar [2], Ali E. Anqi [2] and Nandalur Ameer Ahammad [4]**

1 Department of Mechanical Engineering, Faculty of Engineering, University of Malaya, Kuala Lumpur 50603, Malaysia; abgaphur@siswa.um.edu.my
2 Mechanical Engineering Department, College of Engineering, King Khalid University, Abha 61413, Saudi Arabia; sarfaraz.kamangar@gmail.com (S.K.); aanqi@kku.edu.sa (A.E.A.)
3 Department of Mechanical Engineering, Zakir Hussain College of Engineering and Technology, Aligarh Muslim University, Aligarh 202002, India; ayusmani@zhcet.ac.in
4 Department of Mathematics, Faculty of Science, University of Tabuk, Tabuk 71491, Saudi Arabia; anaudalur@ut.edu.sa
* Correspondence: nik_nazri@um.edu.my (N.N.N.G.); magami.irfan@gmail.com (I.A.B.)



**Citation:** Athani, A.; Ghazali, N.N.N.; Badruddin, I.A.; Usmani, A.Y.; Kamangar, S.; Anqi, A.E.; Ahammad, N.A. Two-Phase Non-Newtonian Pulsatile Blood Flow Simulations in a Rigid and Flexible Patient-Specific Left Coronary Artery (LCA) Exhibiting Multi-Stenosis. *Appl. Sci.* **2021**, *11*, 11361. https://doi.org/10.3390/app112311361

Academic Editors: Qi-Huang Zheng, Gionata Fragomeni and Vera Gramigna

Received: 3 September 2021
Accepted: 27 October 2021
Published: 1 December 2021



**Abstract:** Coronary artery disease (CAD) is stated as one of the most common causes of death all over the world. This article explores the influence of multi stenosis in a flexible and rigid left coronary artery (LCA) model using a multiphase blood flow system which has not yet been studied. Two-way fluid–solid interaction (FSI) is employed to achieve flow within the flexible artery model. A realistic three-dimensional model of multi-stenosed LCA was reconstructed based on computerized tomography (CT) images. The fluid domain was solved using a finite volume-based commercial software (FLUENT 2020). The fluid (blood) and solid (wall) domains were fully coupled by using the ANSYS Fluid-Structure Interaction solver. The maximum pressure drops, and wall shear stress was determined across the sever stenosis (90% AS). The higher region of displacement occurs at the pre-stenosis area compared to the other area of the left coronary artery model. An increase in blood flow velocity across the restricted regions (stenosis) in the LCA was observed, whereas the recirculation zone at the post-stenosis and bifurcation regions was noted. An overestimation of hemodynamic descriptors for the rigid models was found as compared to the FSI models.

**Keywords:** left coronary artery (LCA); pulsatile blood flow; arterial stenosis (AS); computed tomography (CT); computational fluid dynamics (CFD); fluid structure interaction (FSI); hemodynamics

## 1. Introduction

Worldwide, cardiovascular diseases (CVDs) constitute the major cause of mortality and morbidity. Ischemic heart disease and stroke were the world's top fatalities for the last 15 years, according to WHO data, with a total 15.2 million fatalities in 2016 [1]. Atherosclerosis, the leading cause of cardiovascular disease, can express itself in a variety of ways, including myocardial ischemia, hemorrhagic stroke, and peripheral arterial disease [2]. It is a chronic inflammatory disorder involving multiple cells such as endothelial cells (ECs), monocytes, and VSMC (vascular smooth muscle cells), monocyte-derived macrophages, dendritic cells, and regulatory T cells (TREG). Biomedically, it is defined as the existence of "cholesterol-engorged" (fat) macrophages in arterial atherosclerotic plaques [3]. Endothelial cells could be activated and in turn release adhesive molecules; ICAM-1 (Inter-Cellular Adhesion Molecule-1) and VCAM-1 (Vascular Cell Adhesion Molecule-1), under the influence of several factors namely: disturbed blood flow, greater plasma low density lipoprotein (LDL) compositions, pathogens from bacterial antigens, cigarette smoke (VCAM-1) and

high blood pressure (HBP). This leads to thrombus formation in large and medium-sized arteries such as a coronary artery [4–6]. Atherosclerotic lesions tend to deposit at multiple locations within the coronary artery, and this then results in hemodynamic disturbances that restrict the flow of blood to the tissues [7] creating a situation of flow impediment. Disturbed blood flow patterns generate signatures of altered hemodynamic wall loading that essentially forces the patient to face higher health risks.

Employing computational fluid dynamics (CFD) together with medical imaging techniques, such as, magnetic resonance imaging (MRI), computed tomography (CT), and echocardiography has become an efficient tool in the recent past, to investigate the hemodynamics within multiple stenosed coronary arteries [8]. Moreover, earlier studies claimed that blood flow, especially in stenosed arteries, cannot be considered a single-phase homogeneous viscous fluid [7,9,10] and instead employs a multiphase model. The more realistic multiphase model provides more information, such as, RBC volume fraction (VF), RBC velocity, viscosity of RBC and plasma [11]. Fewer studies incorporating a multiphase model while considering a real geometry model from an 8-year-old female patient with a moderate coarctation of aorta (CoA) [12], idealized geometric arteries [13–15] and pulsatile blood flow in coronary arteries [11,16] have been reported. Additionally, the mechanism of atherogenic disease progression is somewhat complex, so the hemodynamic indicators arising from multiphase modelling serve as bio markers for healthcare providers [17]. Researchers have reported for ideal as well as patient-specific models that the regional wall shear stress (WSS) and oscillatory shear index (OSI) play a critical and fundamental role in the progression of atherosclerosis [14,18,19]. These indicators are significantly linked to the prediction or development of atherosclerosis in arteries as they tend to alter; the structure of endothelial cell layer in the surrounding tissues, and the relationship between biomechanical stresses or deformation [20,21]. In a flexible artery, exhibiting single and double stenoses [22], showed that laminar flow occurs for a 70% stenosis while, the flow becomes turbulent for 80% occlusion. Additionally, dilation in the arterial walls in double stenoses was found to be more common than in single stenosis. This in turn, caused a suppression in the maximum mean WSS value in a double stenosis, compared to single stenosis. More details of CFD fluid–solid interaction (FSI) studies are available in the literature [19–21,23–26], respectively. Furthermore, an atherosclerotic condition develops near bifurcations as well as areas of highest curvature in the arteries, as they result in blockage of blood supply in the myocardium [23,27]. However, there are no studies conducted using multiphase blood flow incorporating fluid–solid interactions in a patient-specific left coronary artery (LCA).

The primary basis of this manuscript is to assess the flow dynamics in a patient-specific model carrying multi-stenosis. Furthermore, the walls of the artery are assumed to be flexible and multiphase modelling is incorporated in the artery. The presence of single stenosis is common in a LCA and has been addressed by several researchers. The existence of multi-stenosis may occur due to alterations in blood flow owing to the already present stenosis in an artery. The growth of new stenotic lesions at multiple places are a major cause of patient fatalities. Additionally, the motivation behind this study is use of the side branch arteries i.e., LAD and left circumflex (LCx) in the model that other authors have used to a very limited extent. This study aims to provide more realistic details to comprehend the blood flow behavior while incorporating wall deformation.

## 2. Materials and Methods

### *2.1. Data Acquisition and Processing*

The CT data were chosen for a suspected coronary artery disease (CAD) male patient aged 46, for the development of 3D-left coronary artery (LCA) models. A specific procedure was followed to obtain clear CT scanned images of the patient. The reorganization period was set 0.6 mm, and the beam collimation of 0.6 with a pitch of 1.4, a tube voltage of 100 kVp, and a current span between 300 and 650 mAs. The images were reconstructed axially with a slice thickness of 0.6 mm and an accumulative distance of 0.75 mm. More

than 400 slices were used to create images in all directions of sagittal, coronal, and axial planes. The data were acquired in standard DICOM formats, and a realistic 3D left coronary artery model was reconstructed using CT volume data and image processing software MIMICS (Materialise HQ Technologielaan 15, Leuven, Belgium), also used in earlier studies [20,28,29].

The multiple stenoses were conceived as the main objective of the present study. MIMICS 18 software used to export the CT scan images obtained from the patient. The left coronary artery model reconstructed was accomplished by identifying appropriate thresholds ranging from 84 to 630 HU. The left coronary artery was positioned, and the segmentation procedure was performed as shown in Figure 1a.

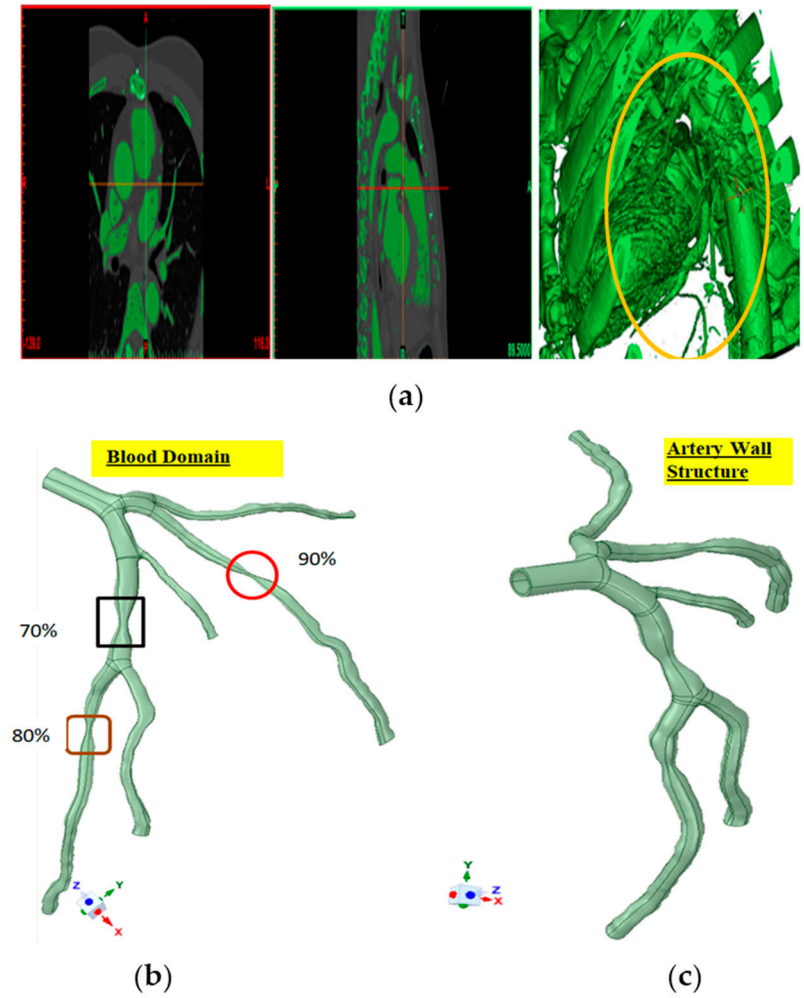


**Figure 1.** (**a**) Computed Tomography (CT) images left, right, posterior, interior, and volume rendering image with actual location of the left coronary artery (LCA). (**b**) Stereo-lithography (.stl) model obtained from MIMICS software. (**c**) Artery wall structure developed in ANSYS.

Furthermore, a pulsatile inlet (Figure 2) was enforced at the model inlet. The pulsatile inlet velocity is applied at the inlet of the model, the physiology of blood flow in the left coronary artery was chosen from previously published articles [14,20,30]. Furthermore, an "outflow" boundary condition was imposed at the respective outlets of the LCA model. Moreover, the inlet diameter was 3.186 mm, while the left main (LM) length considered in simulations was 19.11 mm which was sufficient (i.e., six diameters) for the flow to become fully developed prior to stenosis. Numerical simulations were carried out in a LCA model for a total of 750 steps. A constant time step of 0.005 s was chosen with 20 iterations in each time-step. Total calculation time amounted to 3.75 s. The convergence of continuity

and momentum was considered as $10^{-4}$. The results presented in the manuscript were revealed at the end of the third simulation cycle.

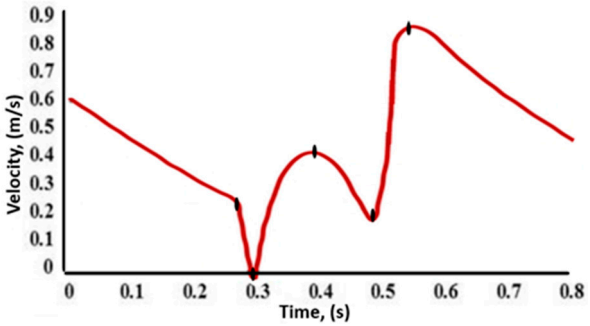


**Figure 2.** Inlet pulsatile blood flow in the left coronary artery (LCA) model [20].

### 2.2. Material Properties

The structural properties of the arterial wall required for establishing FSI simulations are perceived from Eslami et al. [24]. Moreover, the fluid properties mimicking blood composed of blood plasma and RBC are adopted from an earlier study [16]. These are further listed in Table 1.

**Table 1.** Properties of blood plasma, RBC and structural properties of artery wall [16,24].

| Parameters | Value |
|---|---|
| Primary Phase | |
| Density of Plasma ($\rho_p$) | 1003 kg/m$^3$ |
| Viscosity | 0.0013 kg/m-s |
| Secondary Phase | |
| RBC (Red Blood Cells) Density ($\rho_{RBC}$) | 1096 kg/m$^3$ |
| Granular diameter of RBC | 8 µm |
| RBC volume fraction | 0.45 |
| Coefficient of Restitution, (e) | 0.99999 |
| Coefficient of Wall restitution ($e_w$) | 0.9999 |
| Coefficient of Specularity ($\varphi$) | 0.60 |
| packing limit of RBC, $(\varepsilon_s)_{max}$ | 0.70 |
| Viscosity model | Carreau model |
| Time Constant ($\lambda$) [s], | 3.313 |
| Index of Power-Law ($n$) | 0.3568 |
| Zero shear viscosity ($\mu_0$) | 0.056 (kg/m-s) |
| Infinite shear viscosity ($\mu_\infty$) | 0.00345 (kg/m-s) |
| Structural Properties | |
| Artery Wall Density($\rho_s$) | 1300 kg/m$^3$ |
| Wall thickness | 0.5 mm |
| Young's Modulus | 1.08 (MPa) |
| Poisson's ration($\upsilon$) | 0.49 |
| Bulk Modulus | $1.8 \times 10^7$ (Pa) |
| Shear Modulus | $3.6242 \times 10^5$ (Pa) |

### 2.3. Development of 3D Models for Simulation (Computational Fluid Dynamics (CFD) and Fluid–Solid Interaction (FSI))

Numerical analysis tool ANSYS version 2020R$_1$ was used to import the reconstructed 3-dimensional stereo lithographic (.stl) model, as shown in Figure 1b. However, the FSI model was constructed of fluid and solid domains representing blood and the wall respectively, later developed using ANSYS, are shown in Figure 1b,c.

The elastic wall of 0.5 mm thickness was generated by referring to the previously published manuscript [24] using the blood domain volume model. The geometrical details of the LCA revealed in Figure 3 had dimensions given in Table 2.

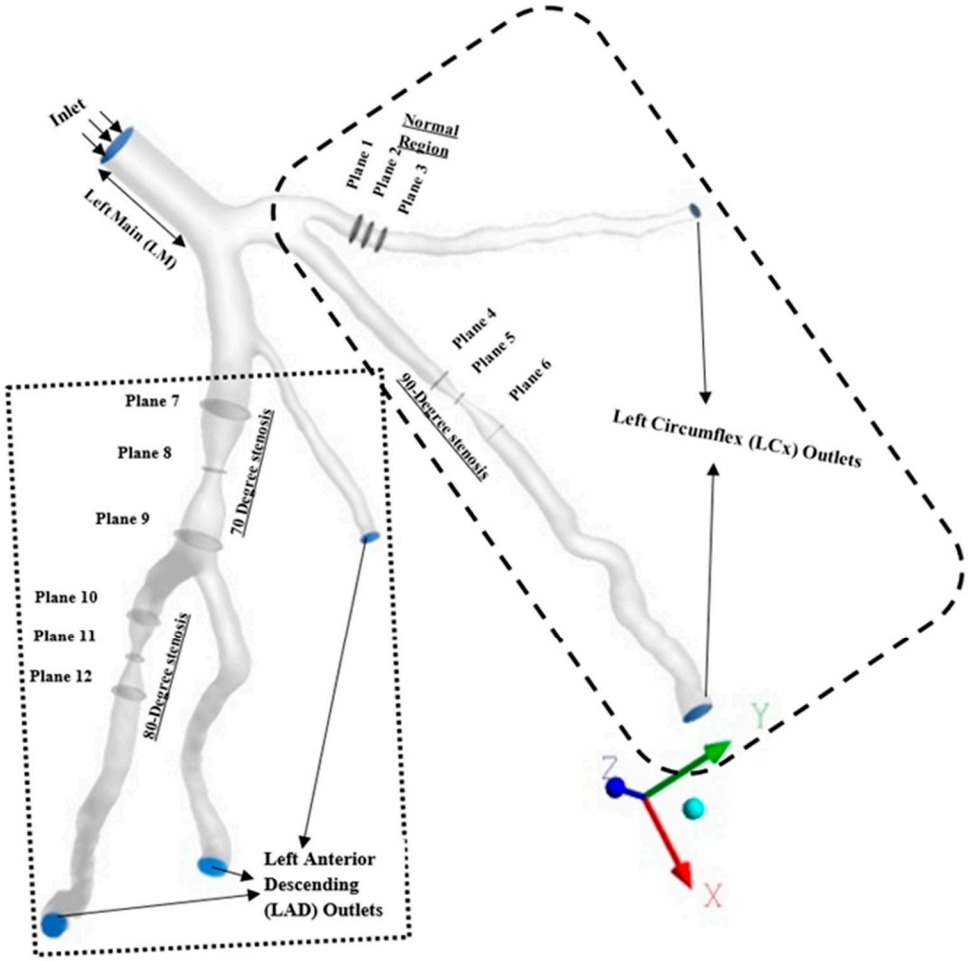


**Figure 3.** Geometrical details of Left anterior descending (LAD) and left circumflex (LCx) branches with cross-sectional (CS) planes at stenosis regions of Left Coronary artery (LCA).

**Table 2.** Geometrical details of actual patient left coronary artery (LCA) model.

| Parameters | Dimensions |
|---|---|
| Length of Left Main (LM) | 9.91 mm |
| Length of left circumflex (LCx) | 66.27 mm |
| Length of Left anterior descending (LAD) | 82.29 mm |
| Vessel wall thickness | 0.5 mm |
| Diameter of LM along Inlet | 3.186 mm |
| Diameter of LAD along Outlet | 2.168 mm |
| Diameter of LCx along Outlet | 2.823 mm |
| Area of inlet (LM) | 7.9715 $mm^2$ |
| Angulation between LCx and LAD | 78.48° |

The 3D-blood domain and artery wall models were meshed separately, and their interface between fluid-solid domain is shown in Figure 4.

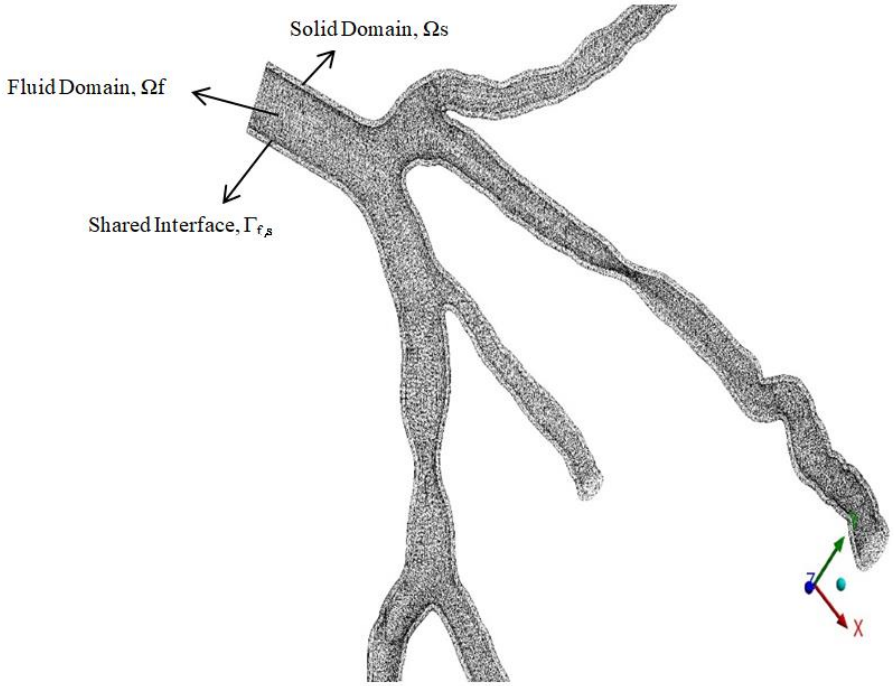


**Figure 4.** Fluid structure Interaction domains and boundary interfaces.

*2.4. Computational Fluid Dynamics (CFD) Model*

In this section, the computational fluid dynamics governing equations are discussed with complete information for the fluid flow system. Commercially available finite volume software ANSYS Fluent was used in the present study for the CFD simulation. The simulation is subdivided into many mechanism volumes to be related to finite volume method. The conservation equation applicable is given [31] as in Equation (1).

$$\int_{CV} \frac{\partial(\rho\varphi)}{\partial(t)} dV + \int_{CV} \nabla\cdot(\rho\varphi u) dV = \int_{CV} \nabla\cdot(\Gamma\nabla\varphi) dV + \int_{CV} S_\varphi dV \quad (1)$$

where, $\rho$ is density, $\varphi$ is a variable fluid property, $CV$ is the control volume, $\Gamma$ is the diffusion coefficient, and $S_\varphi$ is the rate of increase of the property $\varphi$ due to sources.

The volume integral of the convective and diffusive terms (Gauss's divergence) is rewritten as,

$$\int_{CV} \nabla\cdot(a) dV = \int_{A} n\cdot a dA \quad (2)$$

where, $n\cdot a$ is the component of vector "a" in the direction of the vector "$n$" normal to surface element "$dA$". So, the Equation (1) can be written as,

$$\frac{\partial}{\partial t}\left(\int_{CV} \rho\varphi dV\right) + \int_{A} n\cdot(\rho\varphi u) dA = \int_{A} n\cdot(\Gamma\nabla\varphi) dA + \int_{CV} S_\varphi dV \quad (3)$$

Here, the terms $\frac{\partial}{\partial t}\left(\int_{CV} \rho\varphi dV\right)$ represents the rate of change of the total amount of fluid property. $\int_{A} n\cdot(\rho\varphi u)$ expresses the net rate of decrease of fluid property $\varphi$ of the fluid element due to convection. $\int_{A} n\cdot(\Gamma\nabla\varphi)$ is the net rate of increase of fluid property $\varphi$ of the fluid elements due to diffusion and $\int_{CV} S_\varphi dV$ is the rate of increase of property $\varphi$ as a result of sources inside the fluid element.

### 2.5. Multiphase Blood Flow Model

The results within the CFD field have a well-established principle in the analysis of multiphase flow. Therefore, the blood was treated as a multiphase abiotic medium consisting of plasma and RBC, as already specified in Section 2.4. The model preserved the volume fraction (VF) of all phases equal to one, as shown in Equation (4).

$$\varepsilon_{plasma} + \varepsilon_{RBC} = 1 \tag{4}$$

where, "$\varepsilon$" is the volume fraction for each phase and the subscripts plasma and RBC are defined over the resultant of the plasma and RBCs, respectively. Multiphase mixture theory was used to examine the hemodynamic parameters because this approach is more precise than the Euler–Euler model as mentioned by an earlier study [32]. Additionally, readers are requested to refer to the literature by [33,34].

### 2.6. Continuity Equation for Multiphase Blood Flow

The continuity equations for mixture theory model are given by,

$$\frac{\partial}{\partial t}(\rho_m) + \nabla\cdot\left(\rho_m \vec{V_m}\right) = 0 \tag{5}$$

$$\vec{V_m} = \frac{\left(\sum_{k=1}^{n} \varepsilon_k \times \rho_k \times \vec{V_k}\right)}{\rho_m} \tag{6}$$

$$\rho_m = \sum_{k=1}^{n} \varepsilon_k \times \rho_k \tag{7}$$

where, $\vec{V_m}$, $\rho_m$ and $\varepsilon_k$ are the mass-averaged velocity, mixture density and hematocrit of phase '$k$' respectively. The sum of all the hematocrits must be given as one for each different phase as stated in the Equation (4). Hence, it has been shown by Equation (8) as,

$$\sum_{k=1}^{n} \varepsilon_k \times \rho_k = 1 \tag{8}$$

### 2.7. Momentum Equation

For each phase, "$k$ is the ratio of plasma over RBCs" and then, the momentum equation becomes,

$$\begin{aligned}\tfrac{\partial}{\partial t}\left(\rho_m \vec{V_m}\right) + \nabla\cdot\left(\rho_m \vec{V_m}\vec{V_m}\right) = -\nabla p + \nabla\cdot\left[\mu_m\left(\nabla\vec{V_m} + \nabla\vec{V_m}^{T}\right)\right] + \\ \left(\rho_m \vec{g}\right) + \left(\vec{F}\right) - \nabla\cdot\left(\sum_{k=1}^{n} \varepsilon_k \rho_k \vec{V_{dr,k}}\vec{V_{dr,k}}\right)\end{aligned} \tag{9}$$

where, $n$, $\vec{F}$ and $\mu_m$ are related to the number of phases, body force and the mixture viscosity respectively and $\mu_m$ is generally expressed as,

$$\mu_m = \sum_{k=1}^{n} \varepsilon_k \mu_k \tag{10}$$

whereas, $\vec{V_{dr,k}}$ is the secondary phase ($k$) drift velocity, which is usually notated by equation,

$$\vec{V_{dr,k}} = \vec{V_k} - \vec{V_m} \tag{11}$$

The drift velocity is active when one of the two phases is created by the particles. In momentum equations, they are overlooked due to the most negligible impact of buoyancy forces and external forces such as rotational, virtual mass, electrical, and shear rise on the blood. The compactness of the blood mixture or blood density is determined by the sum of

the weighted plasma volume fraction and the viscosity of *RBCs* that ignore the blood-borne components of infants, by the following equation:

$$\rho_{mix} = \varepsilon_{plasma}\rho_{plasma} + \varepsilon_{RBC}\rho_{RBC} \tag{12}$$

*2.8. Slip and Drift Velocity*

The slip velocity is defined as the velocity of the secondary phase (expressed as '$p$') relative to the velocity of the primary phase (expressed as '$q$') given by the following equation:

$$\vec{V_{pq}} = \vec{V_p} - \vec{V_q} \tag{13}$$

However, the mass fraction can be stated as,

$$C_k = \frac{\varepsilon_k \rho_k}{\rho_m} \tag{14}$$

$\vec{V_{dr,p}}$ and $\vec{V_{pq}}$ are related to the following equation

$$\vec{V_{dr,p}} = \vec{V_{pq}} - \sum_{k=1}^{n} C_k \times \vec{V_{qk}} \tag{15}$$

The relative velocity from literature [35], $\vec{V_{pq}}$ is given as,

$$\vec{V_{pq}} = \frac{\tau_p}{f_d}\frac{(\rho_p - \rho_m)}{\rho_p} \times \vec{a} \tag{16}$$

where, '$\tau_p$' is the reduction time of particles, which is given as,

$$\tau_p = \frac{\rho_p d_p^2}{18\mu_q} \tag{17}$$

where, $d_p$ and $\vec{a}$ are the diameter and acceleration of secondary phase particles respectively, "$f_d$" is the drag force applied by the fluid on spherical particles. An interphase drag principle was introduced for the two components (multiphase) to consider the dragging-by-fluid force exerted on rigid granular particles. The Gidaspow model [16,36] was adopted for the drag force induced between RBCs and plasma to validate the densely dispersed RBCs. The term drag force is generally expressed as below,

$$f_{d(RBC,Plasma)} = C_{RBC}(U_{RBC} - U_{Plasma}) \tag{18}$$

where, $C_{RBC}$ represents the coefficient of momentum exchanges between the two phases, which is normally referred by the Equation (19),

$$C_{RBC} = \frac{3}{4}\frac{C_D}{d_{RBC}}\varepsilon_{RBC}\varepsilon_{Plasma}\rho_{Plasma}|U_{RBC} - U_{Plasma}| \tag{19}$$

$U_{RBC}$ and $U_{Plasma}$ are the phase velocities of RBC and Plasma respectively, '$d_{RBC}$' is the diameter of RBC, that has chosen to be 8 µm by previously published articles [13,14,16]. The Gidaspow model [36] is generally used with the two separate equations for the drag coefficient for thinned and thick particles.

In case for, $\varepsilon_{RBC} < 0.2$ then $C_D$ is represented by an equation

$$C_D = \varepsilon_{RBC}^{-1.65}\max\left[\frac{24}{R_{e_p}}\left(1 + 0.15{R_{e_p}}^{0.687}\right)0.44\right] \tag{20}$$

where, $R_{e_p}$ is the particle modified Reynolds number and which is expressed as the following equation:

$$R_{e_p} = \frac{\rho_{Plasma}\varepsilon_{Plasma}d_{RBC}|U_{RBC} - U_{Plasma}|}{\mu_{Plasma}} \quad (21)$$

If in case, "$\varepsilon_{RBC} > 0.2$", then the momentum exchange coefficient between phases "$C_{RBC}$" is directly expressed by the equation.

*2.9. Constitutive Model*

The representation of the constitutive model is based on the strain rate tensor "$\underline{\underline{\dot{\gamma}}}$" and viscous stress tensor "$\underline{\underline{\tau}}$" which is expressed by the following equation,

$$\underline{\underline{\dot{\gamma}}} = \nabla\vec{V} + \left(\nabla\vec{V}\right)^T \quad (22)$$

The significance of "$\underline{\underline{\dot{\gamma}}}$" and "$\underline{\underline{\tau}}$" are expressed by $\dot{\gamma}$ and $\tau$ respectively as given in Equations (23)–(25),

$$\dot{\gamma} = \sqrt{\frac{1}{2}\Pi_{\dot{\gamma}}} = \sqrt{\frac{1}{2}\underline{\underline{\dot{\gamma}}} : \underline{\underline{\dot{\gamma}}}} \quad (23)$$

$$\tau = \sqrt{\frac{1}{2}\Pi_{\tau}} = \sqrt{\frac{1}{2}\underline{\underline{\tau}} : \underline{\underline{\tau}}} \quad (24)$$

where, $\nabla\vec{V}$, $\vec{V}$ and $\Pi_\tau$ are the velocity-gradient tensor, velocity vector, and stress tensor of the second invariant, whereas superscript "$T$" represents its transpose. For the viscous fluid, constitutive behavior is given according to the following equation,

$$\tau = \mu\underline{\underline{\dot{\gamma}}} \quad (25)$$

where, "$\mu$" represents the dynamic viscosity of blood. It may be noted that Equations (4)–(25) have been adopted from literature [14]. In the present study, blood was assumed to be two separates fluids, and RBC behaves as a non-Newtonian Carreau model. The detailed rheological properties of blood are given in Table 1. Blood viscosity $\mu$ (kg/m-s) as a function of shear rate $\dot{\gamma}$ (in $s^{-1}$), was considered by the following equation,

$$\mu = \mu_\infty + (\mu_0 - \mu_\infty)\left[1 + (\lambda\dot{\gamma})^2\right]^{\left(\frac{(n-1)}{2}\right)} \quad (26)$$

## 3. Artery Deformation Modelling

In above Figure 4, that shows a systematic FSI problem with a solid $\Omega_s$ and fluid domain $\Omega_f$, which are self-governing from each other and interrelate alongside with common shared interface, $\Gamma_{f,s}$.

The governing wall deformation of a vessel equation is given as,

$$\rho_s\frac{\partial^2 u}{\partial t^2} - \nabla\overline{\overline{\sigma}} = \rho_s\vec{b} \quad (27)$$

where $\rho_s$ is the structure density, $u$ represents the solid displacements, $\overline{\overline{\sigma}}$ represents the Cauchy stress tensor and the body forces applied on the structure are represented by $\vec{b}$, So, the stress tensor for an isotropic linear elastic materials becomes,

$$\overline{\overline{\sigma}} = 2\mu_L\overline{\overline{\varepsilon}} + \lambda_L tr\left(\overline{\overline{\varepsilon}}\right)I \quad (28)$$

where, "$\lambda_L$" and "$\mu_L$" are the first and second-order Lame parameters respectively, $\overline{\overline{\varepsilon}}$ is the strain tensor, "$tr$" represents the trace function, and letter "I" represents the characteristics

matrix. As we know, for any compressible materials, Lame parameters can be generally given as a function of the elastic modulus $E$, and Poisson's ratio $\nu$.

$$\mu_L = \frac{E}{2(1+\nu)} \tag{29}$$

$$\lambda_L = \frac{\nu E}{(1+\nu)(2\nu-1)} \tag{30}$$

### 3.1. Fluid–Structure Interaction (FSI) Modelling

FSI coupling was performed by constructing two separate models that comprised the fluid and the structural domain. In solving the FSI problems, neither Eulerian nor the Lagrangian formulations were primes to both the domain. Lagrangian equation cannot handle large deformations for fluid systems, whereas Eulerian formulation compromises accuracy when applied to the solid domain. Generally, the FSI was resolved using a standard arbitrary Lagrangian–Eulerian (ALE) formulation [37]. The fluid domain is permitted to deform arbitrarily in the ALE method so that its boundaries follow the structural domain's deformation [38]. These two methods were combined and used to solve the structural problems by Lagrangian formulation. The fluid domain and structural domain two-way coupling were attained by using commercial computational software ANSYS FLUENT and ANSYS Structural (ANSYS Inc., Canonsburg, PA, USA) of version $2020R_1$. ANSYS Mechanics uses a finite-element method to solve the structural domain, and ANSYS FLUENT is finite-volume-based software for computational fluid mechanics analysis. In this research, the fluid and solid are both coupled in a two-way system and solved iteratively within each specified time step of 0.005 by applying appropriate conditions at the fluid–structure interface until the system's residual is lower than a specified tolerance.

The FSI problems have the conservation of mass and momentum along with the interfaces [39]. These values are content of the displacement compatibility and traction equilibrium at $\Gamma_{f,s}$,

$$\vec{u_{f,\Gamma}} = \vec{u_{s,\Gamma}} \tag{31}$$

$$\vec{t_{f,\Gamma}} = \vec{t_{s,\Gamma}} \tag{32}$$

In the above equations, where $\vec{u_{f,\Gamma}}$ is defines the fluid displacement at the interface and $\vec{u_{s,\Gamma}}$ define the solid displacement at the interface in Equations (31) and (32). Similarly, the forces of the fluid and solid on the interfaces is defined as $\vec{t_{f,\Gamma}}$ and $\vec{t_{s,\Gamma}}$ respectively in Equation (33) is frequently transcribed in stress tensor as,

$$\overline{\overline{\sigma}} \cdot \vec{n_{s,\Gamma}} = -\overline{\tau} \cdot \vec{n_{f,\Gamma}} \tag{33}$$

where, $\overline{\overline{\sigma}}$ is the stress tensor, $\vec{n_{f,\Gamma}}$ and $\vec{n_{s,\Gamma}}$ are the fluid and solid normal interfaces respectively. Equations (27)–(33) have been adapted from previously published articles [20,40].

### 3.2. Wall Shear Stress (WSS)

The WSS is the most crucial parameter in hemodynamic simulation in vessels. The endothelial cells were aligned in the direction of blood flows. These are used to calculate the wall shear stresses in blood vessels. The expression used to calculate the WSS in blood arteries is given as,

$$\tau = \mu \frac{\partial u}{\partial y} = \mu \dot{\gamma} \tag{34}$$

where, WSS ($\tau$) is the wall shear stress in (Pa) and, $\mu$ is the dynamic viscosity, $\frac{\partial u}{\partial y}$ velocity gradient at the wall.

## 4. Mesh Independent Study

An automatic meshing algorithm was selected in the first phase to obtain the discretized fluid-structure domain in ANSYS Meshing. The Tetrahedron mesh method was used to obtain a smooth and uniform mesh. The fluid domain meshed with 727,223 tetrahedral elements and the structural domain with the 157,502 elements. Thus, a total of 884,725 tetrahedral mesh elements were used in the fluid–structure interaction, as depicted in Figure 4.

Furthermore, the mesh was refined by adding the inflation layers across the interface between the fluid and structural domains to obtain more precise results in areas near the artery walls. An independent grid study was also performed, as described in Figure 5. The simulations were started while considering 213,195 elements, these grids were then successively increased until the independence was achieved at 884,725 elements. The pressure value stabilized beyond the chosen grid.

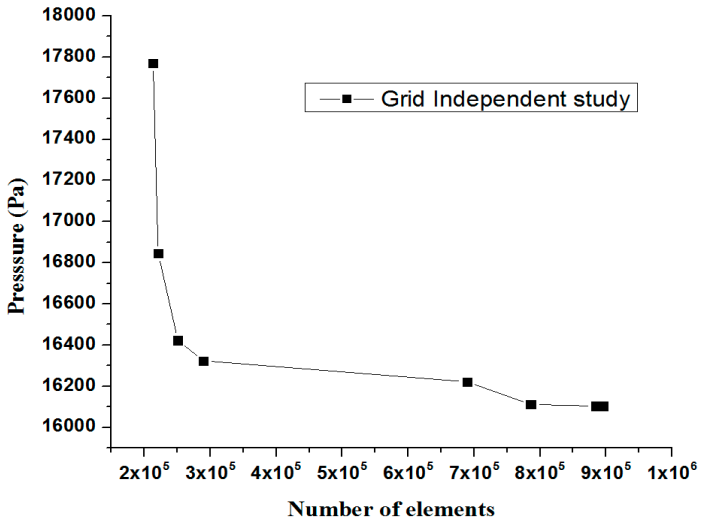


**Figure 5.** Mesh independent study for pressure along the diastolic condition (0.55 s).

## 5. Results and Discussion

The numerical simulation of blood flow in the left coronary artery with multiple stenoses was carried out using multiphase mixture theory. In the current study, hemodynamic parameters such as WSS, pressure, velocity, etc., were evaluated in the patient's left coronary artery and while considering the walls to be rigid and flexible. Subsequently, the results were then compared. As mentioned earlier, the current investigation aims to compare the rigid left coronary artery model with the FSI left coronary artery model.

### *5.1. Wall Pressure*

Figure 6 shows the comparison of the wall pressure between the rigid and FSI model of the left coronary artery at systolic and diastolic phase of the cardiac cycle. The pressure drop was maximum across the 90% area stenosis as compared to other regions of stenosis. The maximum pressure drop was found as 100,077 Pa for both the rigid and FSI models, whereas a slight difference in wall pressure was noted across the bifurcation in both the models. The pressure drop across the 70% and 80% area stenosis were 11,727 Pa and 10,784 Pa, respectively. Similarly, the wall pressure for the CFD and FSI models of the left coronary artery was plotted for the diastolic phase of the cardiac cycle. It can be seen clearly that the wall pressure drop was maximum across the 90% area stenosis present at the LCX branch as compared to 70% and 80% at the LAD branch. It was found that the pressure drops to 8871 Pa across 90% of the area of stenosis for the diastolic phase of the cardiac cycle for both the models. A slight variation across the bifurcation regions was observed in wall pressure between the rigid and FSI models.

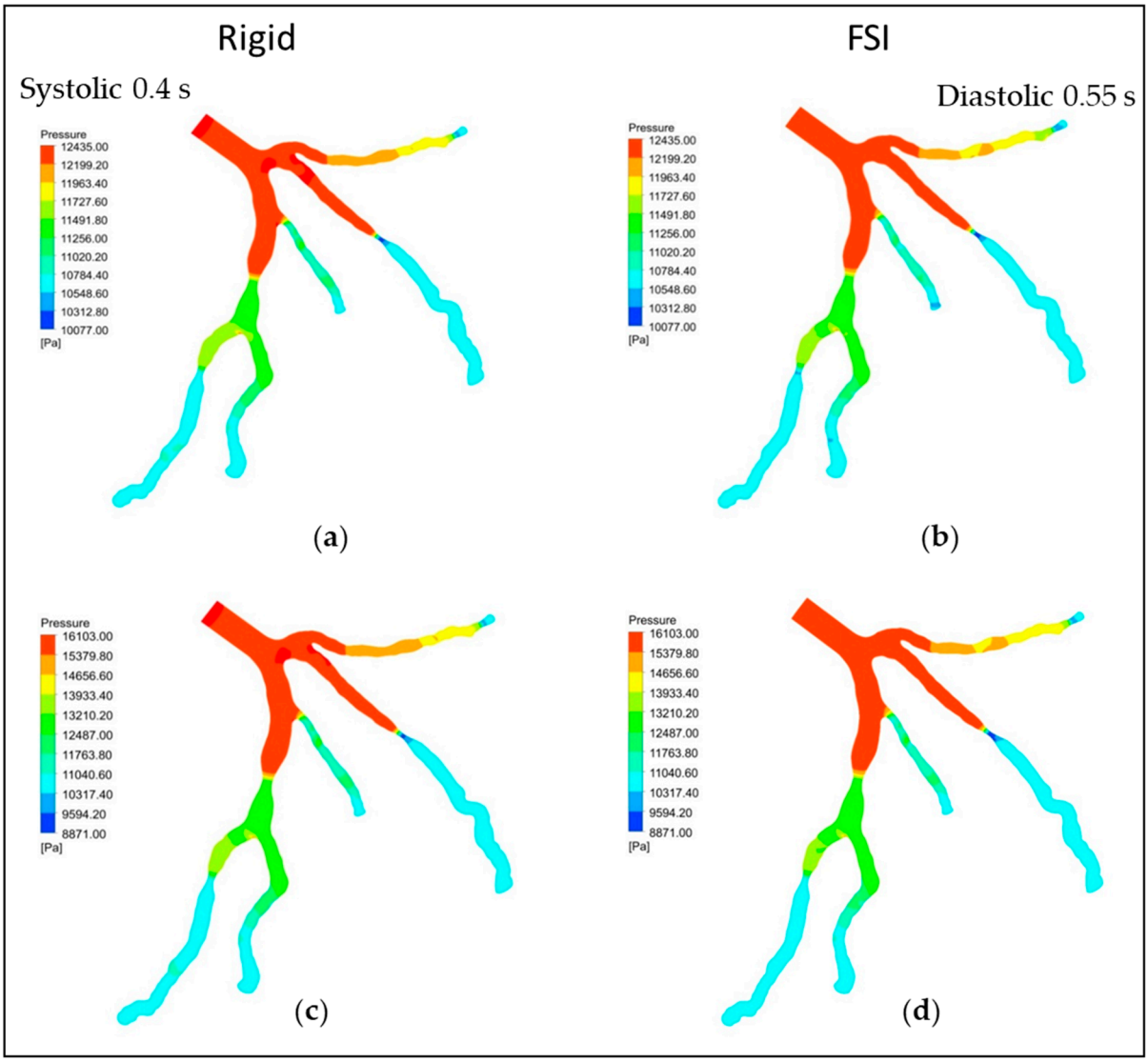


**Figure 6.** Wall pressure field in left coronary artery during the systolic and diastolic phase of cardiac cycle for (**a**,**c**) Rigid and (**b**,**d**) FSI models.

### *5.2. Wall Shear Stress (WSS)*

Figure 7 shows WSS variation for the rigid and FSI models during the systolic and diastolic periods of the cardiac cycle. It can be clearly observed that a significant increase in the WSS was found across 90% of the area of stenosis as compared to 70% and 80% of the area of stenosis. A slight increase in the WSS for the diastolic phase of the cardiac cycle was found across the bifurcation regions compared to the systolic phase of the cardiac cycle. The highest WSS at 90% of the area of stenosis was found in the range 40 to 50 Pa. The wall shear stress plays a substantial role in evaluating the strength of the artery, and it is believed that the higher wall shear stress may assist in a rupture of the artery wall. The overall WSS in the segmented left coronary artery shows a slight variation when comparing the CFD and FSI models. This can be described by the deformation of artery wall, which produces pressure waves that promulgate at a finite speed through the arteries, in contrast to the CFD model with rigid walls which produce instantaneous wave propagation [24].

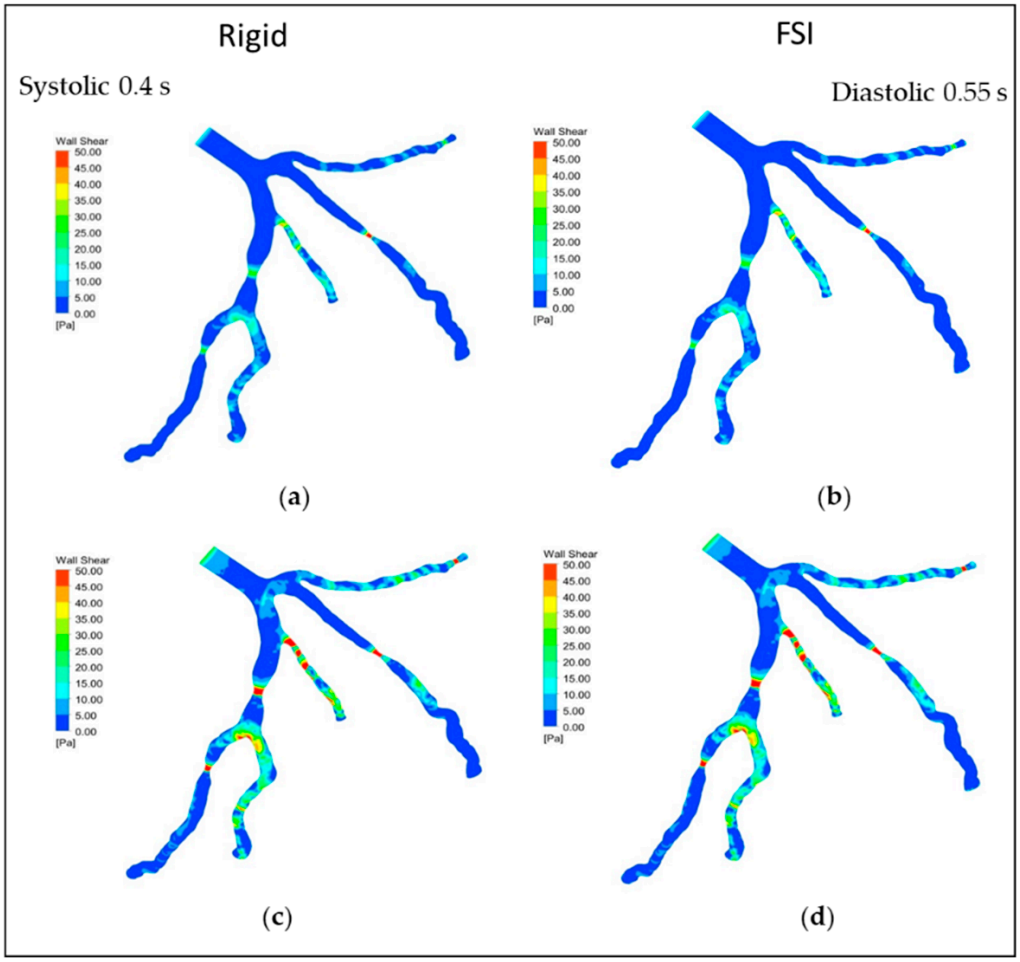


**Figure 7.** Wall shear stress field in the left coronary artery during the systolic and diastolic phase of cardiac cycle for (**a**,**c**) rigid and (**b**,**d**) fluid–solid interaction (FSI) models.

### *5.3. Displacement*

Figure 8 represents the wall displacement contours due to the pressure on the wall in the whole left coronary artery within the FSI model during the systolic and diastolic phases of the cardiac cycle.

The maximum displacement in the range of 2.28–3.26 microns was found at the peak diastolic phase of the cardiac cycle. The higher region of displacement occurs at the pre stenosis region compared to the other region of the entire left coronary artery model. In systole, the displacement region is like that at the peak diastolic phase, but the maximum displacement is much smaller in the range of 0.33–1.3 micron.

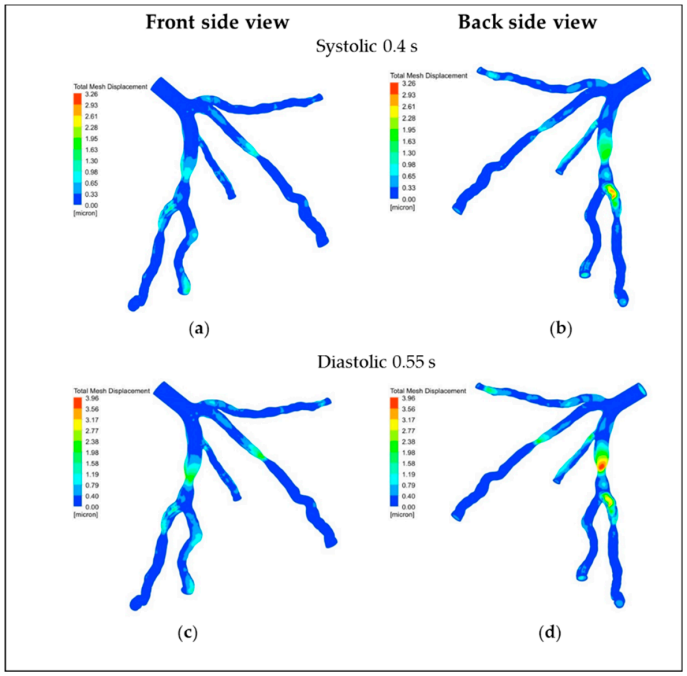


**Figure 8.** Projected displacement patterns on wall of left coronary artery (LCA) at systolic flow for different views—(**a**) front side (**b**) back side, and diastolic flow (**c**) front side (**d**) back side.

### *5.4. Velocity Streamlines*

Figure 9 depicts the velocity streamline of blood flow in the left coronary artery for rigid and FSI models during the cardiac cycle's systolic and diastolic phases. The higher velocity of blood flow can be found across the restricted regions (stenosis) in the left coronary artery.

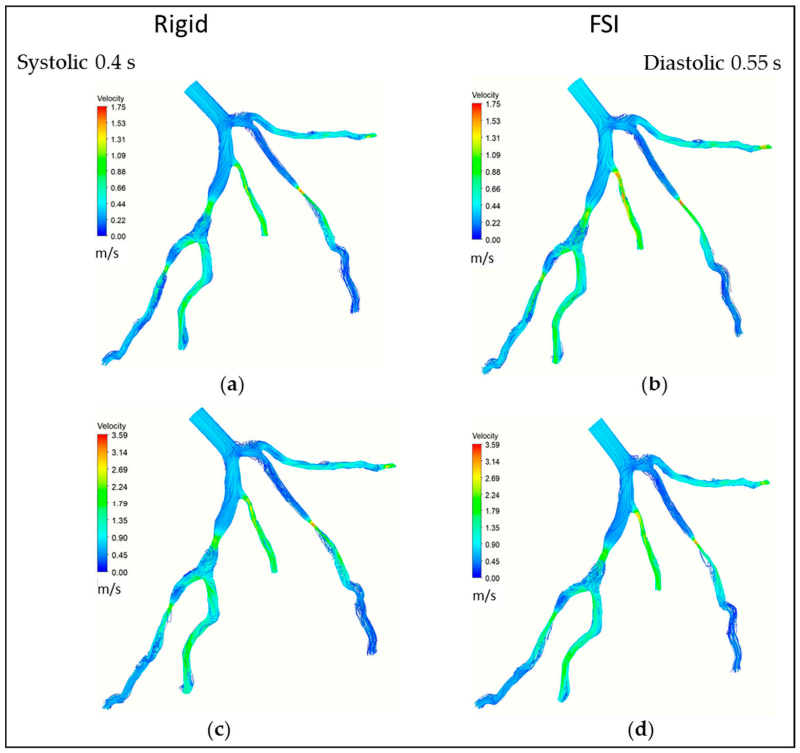


**Figure 9.** Velocity streamlines of the blood flow field in the left coronary artery (LCA) during the systolic and diastolic phase of cardiac cycle for (**a**,**c**) rigid and (**b**,**d**) FSI models.

It was also observed that a significant increase in the velocity was found for the FSI model compared to rigid model, across the stenosis region. The higher velocity varied within 0.78–1 m/s for the rigid wall while a range of 0.45–0.9 m/s was encountered in the FSI model, along the systolic phase of the cardiac cycle. Similarly, the maximum velocity in the range from 1.8–2.25 m/s for the rigid model and 1.81–2.26 m/s for the FSI model was observed during the diastolic phase. A prominent recirculation region at post stenosis region followed by a bifurcation, was observed.

### *5.5. RBC Volume Fraction (VF)*

The two-phase mixture theory model of RBCs and plasma was primarily simulated with 45% hematocrit concentration. The volumetric fraction counters of RBC for the rigid (top) and FSI (bottom) models during the systolic and diastolic phase of the cardiac cycle is shown in Figure 10 on planes 1–12 revealed in Figure 3. The cross-section plans across the normal, pre, mid, and post stenosis for 70%, 80%, and 90% of the area of stenosis were plotted. It was determined that the volume fraction of RBC increases across the stenosis region for the peak diastolic as compared to the systolic phase of the cardiac cycle. The volume fraction of RBCs reduces as the velocity was found to increase at the pre stenosis region compared to the mid and post stenosis region. The wall shear stress across the stenosis region was increased significantly with increases in the RBCs volume fraction which can be observed in Figure 10 for both the rigid and FSI models.

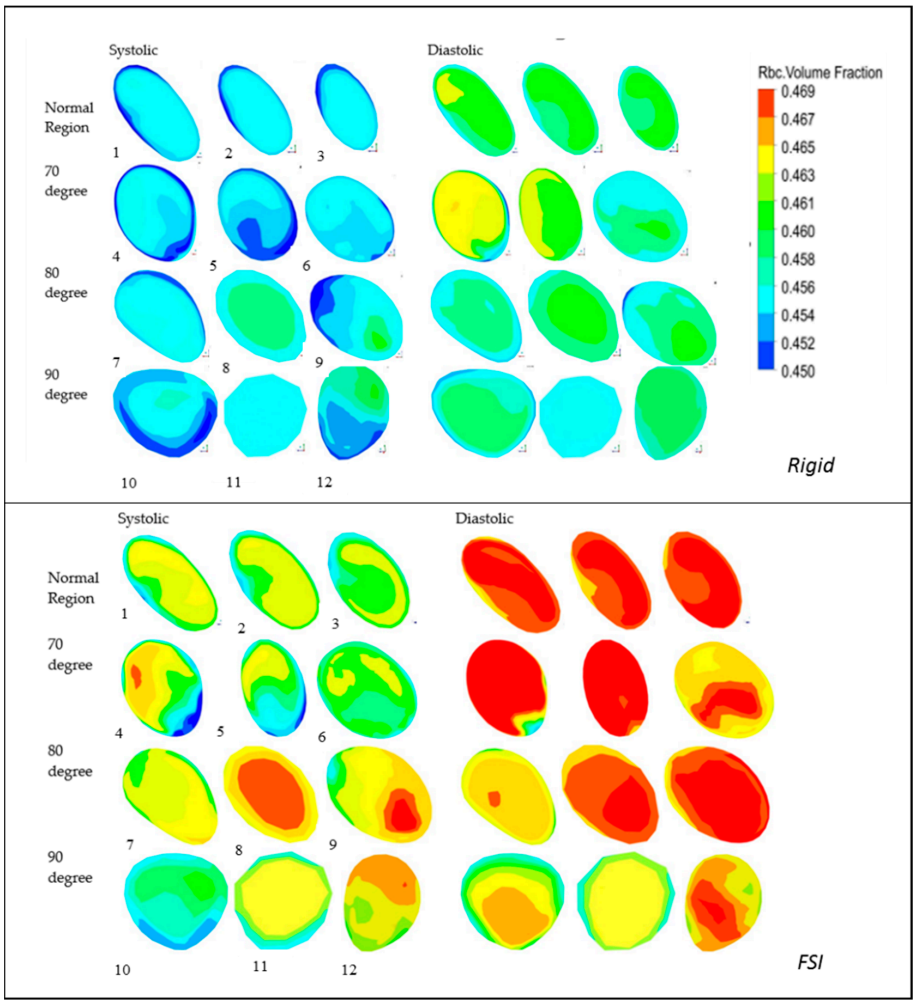


**Figure 10.** RBC volume fraction across the stenosis with degrees: 70%, 80% and 90% in left coronary artery (LCA) during systolic and diastolic phase of cardiac cycle within a rigid model (top) and FSI model (bottom) on planes 1–12.

## 6. Discussion

The current study demonstrates the impact of stenosis located at multiple positions within the left coronary artery (LCA), on hemodynamic indicators. The simulation was performed in a patient specific left coronary artery model while considering the walls to be rigid and flexible in nature, through establishing a two–way FSI approach. A multiphase blood model incorporating a mixture of RBC and plasma is further considered. The results obtained within a rigid walled is compared against a FSI model and has not been previously studied. Left anterior descending (LAD) exhibits a stenosis of 70% and 80% while left circumflex ($LC_X$) encounters a 90% occlusion. The local hemodynamic parameters such as WSS play a significant role in damaging the endothelial cells located on the inner side of the arteries. The WSS and another hemodynamic variable cannot be determined non-invasively. In the past few years, advances in medical imaging techniques such as MRI, CTA, and IVUS have made it possible to differentiate between the wall of the coronary artery and the undesirable deposition but are limited to find the disturbed flow region and oscillatory shear stress regions. The variation in the normal physiologic value of WSS leads to determining the progression and development of atherosclerosis. The simulated results showed that WSS was significantly higher than the physiological value (50 Pa) in the presence of stenosis, and the disturbed flow region was noted across the bifurcations and post-stenotic regions.

The maximum WSS was found across the 90% AS, which was consistent with the previously published literature. The pressure drop increased across the higher degree of stenosis as noted in the previous studies. Bifurcation and post-stenotic regions encounter lower pressure as demonstrated in Figure 6, these are primarily the areas associated with progression and development of stenosis [27,41]. A notable accumulation of RBC at the pre stenosed region was demonstrated by current results in Figure 10, consistent with the previously published literature [13,14] and in turn, essentially contributes to thrombosis [22,42]. The discrepancies of rigid model results are due to overlooking the wall motion that subsequently generates pulse that travels within the flexible model (FSI) which, however, in rigid model is suppressed. Additionally, the contours obtained for pressure, velocity and WSS are qualitatively similar, across rigid and FSI models. However, quantitatively; along the throat of 90% occlusion these are different compared to rigid in the following aspects: (a) the FSI model encounters higher flow velocities during the diastolic portion of the cycle. At systolic phase a 2% decrease in the velocity is encountered while along the diastolic phase, a 3.5% increase in velocity is achieved. (b) The overall pressures based on the average quantity are lower by 5.7% in FSI models due to wall deformations. (c) Along the stenosis, the WSS values are suppressed by 6.5% in flexible models (d) Recirculation regions along the post-stenotic region are smaller in FSI models. The competence of calculating the hemodynamic parameters non-invasively is not only important for the diagnosis of diseases, but also significant for the development of a patient's specific devices to improve the quality of treatment procedure. There are some limitations of this study that should be addressed in future. Firstly, the wall of the artery was modeled with the uniform thickness, which is a common assumption reasoned by previous studies. Secondly, the flow waveform at the model inlet has been adopted from literature studies [14,20,43] while the outlets are assigned an outflow condition, thus the simulated results do not reflect the actual physiological condition. Therefore, the flow and pressure waveforms should be used for that individual patient through a medical hospital to obtain more realistic and precise physiological conditions. Third, the actuation frequencies exhibited within the heart owing to exercise and resting conditions of the patient which has a significant effect on the coronary arteries and the hemodynamic parameters, were not considered. Lastly, a single patient specific left coronary artery model has been used in the current study and, so as to reflect the actual physiological conditions, the study should incorporate more patients and additionally a more complex arterial network should be incorporated in future studies.

## 7. Conclusions

This study explored the impact of various degrees of stenosis located within LAD and LCX branches on the hemodynamic variables for CFD and FSI models. A more realistic blood flow in both models was based on mixture of RBCs in the blood plasma, was employed to study the transport and their interactions. The current numerical simulations were performed with rigid and two-way coupled FSI models and compared the hemodynamic parameters of multi-stenosis LCA. A distinction of simulation result between rigid and fully coupled arterial walls revealed not only significant qualitative differences in WSS distribution, but also notable change in WSS and other hemodynamic features. A significant variation in the blood flow field and a substantial increase in the WSS were found across the 90% AS which may increase the risk of stenosis rupture. The significant increase in the velocity and a recirculation region immediate to the stenosis could lead to the further progression and development of stenosis. Hence, for accurate WSS computations, displacement of artery wall results play an important role. Also, the higher severity of stenosis may require an immediate interventional procedure to cure the disease.

**Author Contributions:** Conceptualization, A.A., N.N.N.G. and I.A.B.; methodology, A.A., N.N.N.G., S.K., A.Y.U.; software, A.A., S.K., A.E.A., A.Y.U.; validation, A.A., N.N.N.G. and I.A.B.; formal analysis, S.K., A.E.A.; investigation, A.A., S.K.; resources, A.E.A., A.Y.U., N.A.A.; data curation, A.A., A.Y.U., N.A.A.; writing—original draft preparation, A.A., N.N.N.G.; writing—review and editing, I.A.B., A.E.A., A.Y.U., N.A.A.; visualization, A.A., I.A.B., A.Y.U.; Funding acquisition: I.A.B., S.K., N.N.N.G., N.A.A.; supervision, N.N.N.G., I.A.B.; project administration, N.N.N.G., I.A.B. All authors have read and agreed to the published version of the manuscript.

**Funding:** King Khalid University under grant number 1/327/42. and University of Malaya grant number GPF020A-2019.

**Institutional Review Board Statement:** Not applicable.

**Informed Consent Statement:** Not applicable.

**Acknowledgments:** The authors extend their appreciation to the Deanship of Scientific Research at King Khalid University for funding this work through the research groups program under grant number RGP.1/327/42. Authors also thank University of Malaya for supporting the work under grant number GPF020A-2019.

**Conflicts of Interest:** The authors declare no conflict of interest.

## References

1. Benjamin, E.J.; Virani, S.S.; Callaway, C.W.; Chamberlain, A.M.; Chang, A.R.; Cheng, S.; Chiuve, S.E.; Cushman, M.; Delling, F.N.; Deo, R. Heart disease and stroke statistics—2018 update: A report from the American Heart Association. *Circulation* **2018**, *137*, e67–e492. [CrossRef] [PubMed]
2. Hansson, G.K.; Robertson, A.-K.L.; Söderberg-Nauclér, C. Inflammation and atherosclerosis. *Annu. Rev. Pathol. Mech. Dis.* **2006**, *1*, 297–329. [CrossRef]
3. Ross, R. Atherosclerosis—An inflammatory disease. *N. Engl. J. Med.* **1999**, *340*, 115–126. [CrossRef]
4. McLaren, J.E.; Michael, D.R.; Ashlin, T.G.; Ramji, D.P. Cytokines, macrophage lipid metabolism and foam cells: Implications for cardiovascular disease therapy. *Prog. Lipid Res.* **2011**, *50*, 331–347. [CrossRef]
5. Gerszten, R.E.; Tager, A.M. The monocyte in atherosclerosis—Should I stay or should I go now? *N. Engl. J. Med.* **2012**, *366*, 1734–1736. [CrossRef] [PubMed]
6. Bongo, J.B.; Peng, D.Q. The neuroimmune guidance cue netrin-1: A new therapeutic target in cardiovascular disease. *J. Cardiol.* **2014**, *63*, 95–98. [CrossRef]
7. Vlachopoulos, C.; O'Rourke, M.; Nichols, W.W. *McDonald's Blood Flow in Arteries: Theoretical, Experimental and Clinical Principles*; CRC Press: Boca Raton, FL, USA, 2011.
8. Polanczyk, A.; Podgorski, M.; Wozniak, T.; Stefanczyk, L.; Strzelecki, M. Computational fluid dynamics as an engineering tool for the reconstruction of hemodynamics after carotid artery stenosis operation: A case study. *Medicina* **2018**, *54*, 42. [CrossRef] [PubMed]
9. Kopernik, M.; Tokarczyk, P. Development of multi-phase models of blood flow for medium-sized vessels with stenosis. *Acta Bioeng. Biomech.* **2019**, *21*, 63–70. [PubMed]
10. Mallik, B.B.; Nanda, S.; Das, B.; Saha, D.; Das, D.S.; Paul, K. A non-newtonian fluid model for blood flow using power-law through an atherosclerotic arterial segment having slip velocity. *Int. J. Pharm. Chem. Biol. Sci.* **2013**, *3*, 752–760.

11. Jung, J.; Lyczkowski, R.W.; Panchal, C.B.; Hassanein, A. Multiphase hemodynamic simulation of pulsatile flow in a coronary artery. *J. Biomech.* **2006**, *39*, 2064–2073. [CrossRef] [PubMed]
12. Melka, B.; Nowak, M.; Gracka, M.; Adamczyk, W.; Golda, A.; Nowak, A.; Białecki, R.; Rojczyk, M.; Ostrowski, Z. CFD modeling of blood flow in rigid and elastic vessels-multifluid & multiscale approach. In Proceedings of the XXIII Zjazd Termodynamików, Gliwice, Poland, 10 September 2017.
13. Joisar, K.; Bhoraniya, R.; Harichandan, A. Numerical analysis of two-phase blood flow in idealized artery with blockage. In *Innovative Design, Analysis and Development Practices in Aerospace and Automotive Engineering (I-DAD 2018)*; Springer: Berlin/Heidelberg, Germany, 2019; pp. 259–267.
14. Buradi, A.; Mahalingam, A. Effect of stenosis severity on wall shear stress based hemodynamic descriptors using multiphase mixture theory. *J. Appl. Fluid Mech.* **2018**, *11*, 1497–1509. [CrossRef]
15. Wu, W.-T.; Aubry, N.; Antaki, J.F.; Massoudi, M. Simulation of blood flow in a sudden expansion channel and a coronary artery. *J. Comput. Appl. Math.* **2020**, *376*, 112856. [CrossRef] [PubMed]
16. Huang, J.; Lyczkowski, R.W.; Gidaspow, D. Pulsatile flow in a coronary artery using multiphase kinetic theory. *J. Biomech.* **2009**, *42*, 743–754. [CrossRef] [PubMed]
17. Bit, A.; Chattopadhay, H. Acute aneurysm is more critical than acute stenoses in blood vessels: A numerical investigation using stress markers. *BioNanoScience* **2018**, *8*, 329–336. [CrossRef]
18. Wu, X.; von Birgelen, C.; Li, Z.; Zhang, S.; Huang, J.; Liang, F.; Li, Y.; Wijns, W.; Tu, S. Assessment of superficial coronary vessel wall deformation and stress: Validation of in silico models and human coronary arteries in vivo. *Int. J. Cardiovasc. Imaging* **2018**, *34*, 849–861. [CrossRef]
19. Malek, A.M.; Alper, S.L.; Izumo, S. Hemodynamic shear stress and its role in atherosclerosis. *JAMA* **1999**, *282*, 2035–2042. [CrossRef]
20. Athani, A.; Ghazali, N.; Badruddin, I.A.; Kamangar, S.; Anqi, A.E.; Algahtani, A. Investigation of two-way fluid-structure interaction of blood flow in a patient-specific left coronary artery. *Bio-Med. Mater. Eng.* **2021**, 1–18. [CrossRef]
21. Cameron, J.N.; Mehta, O.H.; Michail, M.; Chan, J.; Nicholls, S.J.; Bennett, M.R.; Brown, A.J. Exploring the relationship between biomechanical stresses and coronary atherosclerosis. *Atherosclerosis* **2020**, *302*, 43–51. [CrossRef]
22. Jahangiri, M.; Saghafian, M.; Sadeghi, M.R. Numerical simulation of hemodynamic parameters of turbulent and pulsatile blood flow in flexible artery with single and double stenoses. *J. Mech. Sci. Technol.* **2015**, *29*, 3549–3560. [CrossRef]
23. Ta, H.T.; Truong, N.P.; Whittaker, A.K.; Davis, T.P.; Peter, K. The effects of particle size, shape, density and flow characteristics on particle margination to vascular walls in cardiovascular diseases. *Expert Opin. Drug Deliv.* **2018**, *15*, 33–45. [CrossRef]
24. Eslami, P.; Tran, J.; Jin, Z.; Karady, J.; Sotoodeh, R.; Lu, M.T.; Hoffmann, U.; Marsden, A. Effect of wall elasticity on hemodynamics and wall shear stress in patient-specific simulations in the coronary arteries. *J. Biomech. Eng.* **2020**, *142*. [CrossRef] [PubMed]
25. Gholipour, A.; Ghayesh, M.H.; Zander, A.C.; Psaltis, P.J. In Vivo based biomechanics of right and left coronary arteries. *Int. J. Eng. Sci.* **2020**, *154*, 103281. [CrossRef]
26. Malvè, M.; García, A.; Ohayon, J.; Martínez, M. Unsteady blood flow and mass transfer of a human left coronary artery bifurcation: FSI vs. CFD. *Int. Commun. Heat Mass Transf.* **2012**, *39*, 745–751. [CrossRef]
27. Chaichana, T.; Sun, Z.; Jewkes, J. Computation of hemodynamics in the left coronary artery with variable angulations. *J. Biomech.* **2011**, *44*, 1869–1878. [CrossRef] [PubMed]
28. Kamangar, S.; Badruddin, I.A.; Ahamad, N.A.; Govindaraju, K.; Nik-Ghazali, N.; Ahmed, N.; Badarudin, A.; Khan, T. The influence of geometrical shapes of stenosis on the blood flow in stenosed artery. *Sains Malays.* **2017**, *46*, 1923–1933. [CrossRef]
29. Sakellarios, A.I.; Tsompou, P.; Kigka, V.; Siogkas, P.; Kyriakidis, S.; Tachos, N.; Karanasiou, G.; Scholte, A.; Clemente, A.; Neglia, D. Non-invasive prediction of site-specific coronary atherosclerotic plaque progression using lipidomics, blood flow, and LDL transport modeling. *Appl. Sci.* **2021**, *11*, 1976. [CrossRef]
30. Berne, R.M.; Levy, M.N. *Cardiovascular Physiology, Etc*; The C.V.Mosby Company: Maryland Heights, MO, USA, 1967.
31. Versteeg, H.K.; Malalasekera, W. *An Introduction to Computational Fluid Dynamics: The Finite Volume Method*; Pearson Education: London, UK, 2007.
32. Massoudi, M.; Kim, J.; Antaki, J.F. Modeling and numerical simulation of blood flow using the theory of interacting continua. *Int. J. Non-Linear Mech.* **2012**, *47*, 506–520. [CrossRef]
33. Wu, W.-T.; Aubry, N.; Antaki, J.F.; Massoudi, M. Flow of blood in micro-channels: Recent results based on mixture theory. *Int. J. Adv. Eng. Sci. Appl. Math.* **2017**, *9*, 40–50. [CrossRef]
34. Nowak, M.; Melka, B.; Rojczyk, M.; Gracka, M.; Nowak, A.J.; Golda, A.; Adamczyk, W.P.; Isaac, B.; Białecki, R.A.; Ostrowski, Z. The protocol for using elastic wall model in modeling blood flow within human artery. *Eur. J. Mech.-B/Fluids* **2019**, *77*, 273–280. [CrossRef]
35. Manninen, M.; Taivassalo, V.; Kallio, S. *On the Mixture Model for Multiphase Flow*; Technical Research Centre of Finland: Otaniemi, Finland, 1996.
36. Gidaspow, D. *Multiphase Flow and Fluidization: Continuum and Kinetic Theory Descriptions*; Academic Press: Cambridge, MA, USA, 1994.
37. Hron, J.; Turek, S. A monolithic FEM/multigrid solver for an ALE formulation of fluid-structure interaction with applications in biomechanics. In *Fluid-Structure Interaction*; Springer: Berlin/Heidelberg, Germany, 2006; pp. 146–170.

38. Rugonyi, S.; Bathe, K.-J. On finite element analysis of fluid flows fully coupled with structural interactions. *CMES-Comput. Modeling Eng. Sci.* **2001**, *2*, 195–212.
39. Seo, T. Hemodynamic characteristics in the human carotid artery model induced by blood-arterial wall interactions. *Int. J. Biomed. Biol. Eng.* **2013**, *7*, 215–220.
40. Lopes, D.; Puga, H.; Teixeira, J.; Teixeira, S. Fluid–Structure Interaction study of carotid blood flow: Comparison between viscosity models. *Eur. J. Mech.-B/Fluids* **2020**, *83*, 226–234. [CrossRef]
41. Kamangar, S.; Badruddin, I.A.; Govindaraju, K.; Nik-Ghazali, N.; Badarudin, A.; Viswanathan, G.N.; Ahmed, N.S.; Khan, T.Y. Patient-specific 3D hemodynamics modelling of left coronary artery under hyperemic conditions. *Med. Biol. Eng. Comput.* **2017**, *55*, 1451–1461. [CrossRef] [PubMed]
42. Byrnes, J.R.; Wolberg, A.S. Red blood cells in thrombosis. *Blood J. Am. Soc. Hematol.* **2017**, *130*, 1795–1799. [CrossRef] [PubMed]
43. Berne, R.; Levy, M.N. *Cardiovascular Physiology*; CV Mosby Company: Saint Louis, MO, USA; Maryland Heights, MO, USA, 1967.